Morphogenesis and morphometry of brain folding patterns across species

Sifan Yin[1], Chunzi Liu[1], Gary P. T. Choi[2], Yeonsu Jung[1],
Katja Heuer[3], Roberto Toro[3], L. Mahadevan[1,4,5*]

[1]John A. Paulson School of Engineering and Applied Sciences, Harvard University, Cambridge, MA 02138, USA.
[2] Department of Mathematics, The Chinese University of Hong Kong, Hong Kong.
[3]Institut Pasteur, Université Paris Cité, Unité de Neuroanatomie Appliquée et Théorique, F-75015 Paris, France.
[4]Department of Organismic and Evolutionary Biology, Harvard University, Cambridge, MA 02138, USA.
[5] Department of Physics, Harvard University, Cambridge, MA 02138, USA.
*Corresponding author e-mail: lmahadev@g.harvard.edu.

Abstract

Evolutionary adaptations associated with the formation of a folded cortex in many mammalian brains are thought to be a critical specialization associated with higher cognitive function. The dramatic surface expansion and highly convoluted folding of the cortex during early development is a theme with variations that suggest the need for a comparative study of cortical gyrification. Here, we use a combination of physical experiments using gels, computational morphogenesis, and geometric morphometrics to study the folding of brains across different species. Starting with magnetic resonance images of brains of a newborn ferret, a fetal macaque, and a fetal human, we construct two-layer physical gel brain models that swell superficially in a solvent, leading to folding patterns similar to those seen *in vivo*. We then adopt a three-dimensional continuum model based on differential growth to simulate cortical folding *in silico*. Finally, we deploy a comparative morphometric

analysis of the *in vivo*, *in vitro*, and *in silico* surface buckling patterns across species. Our study shows that a simple mechanical instability driven by differential growth suffices to explain cortical folding and suggests that variations in the tangential growth and different initial geometries are sufficient to explain the differences in cortical folding across species.

Introduction

Although not all brains are folded, in many mammals, the folded cerebral cortex is known to be critically important for brain cognitive performance and highly dependent on the hierarchical structure of its morphology, cytoarchitecture, and connectivity [1, 2, 3]. Brain function is thus related both to the topological structure of neural networks [4], as well as the geometry and morphology of the convoluted cortex [5], both of which serve to enable and constrain neuronal dynamics [3]. Across species, cortical morphologies show a large diversity, as shown in Fig. 1(a) [6, 7]. And within our own species and in model organisms such as the ferret used to study the genetic precursors of misfolding, cortical folding and misfolding are known to be markers of healthy and pathological neurodevelopment, disease and aging [8, 9] (see also (Fig. S1 [10, 11]). Thus a comparative study of cortical folding is essential for understanding brain morphogenesis and functionalization across evolution [3, 12], during development as well as in pathological situations associated with disease.

The development of cortical morphology involves the coordinated and localized expression of many genes that lead to the migration and differentiation of neural stem and progenitor cells [13, 10, 14]. All these biological processes cooperatively generate an expansion of the cortex relative to the underlying white matter and eventually drive cortical folding [15]. While a range of mechanisms have been proposed in the past for the processes leading to folding [16, 17, 18], over the past decade, theoretical and experimental evidence have converged on the primary determinant of folding as a mechanical instability associated with the formation of a localized crease or sulcus [19, 20] driven by differential growth, with iterations and variations that qualitatively explain the brain gyrification [21, 22]. However, combining this mechanistic model with a comparative perspective that aims to quantify the variability of folding patterns across species, or linking it to genetic perturbations that change the relative expansion of the cortex

remain open questions. In a companion paper [11], we address the latter using the ferret as a model organism, while in the current study, we address the former question using a combination of physical experiments with gel swelling, numerical simulations of differential growth and geometric morphometrics to compare brain morphogenesis in the ferret, the macaque, and the human. The species were selected as they have very different brain sizes and folding patterns (Fig. 1(b)) and thus represent different branches in the evolutionary tree, Carnivora, Old World monkeys, and Hominoidea. Furthermore, in all three species, we have access to a time course of the development of the folds, as shown in Fig. 1(c).

Experiments on swelling gel-brains

To mimic the mechanical basis for brain morphogenesis based on the differential growth of the cortex relative to the white matter, we used the swelling of physical gels that mimic the fetal brain developmental process during post-gestation stages. Previously, this principle has been demonstrated for *Homo sapiens* (human) brain development [22, 21]. To demonstrate that the same principle applies to other species, we constructed physical gels from the fetal brain MRI scans for *Macaca mulatta* (rhesus macaque) and *Mustela furo* (ferret). In brief, a two-layer PDMS gel is constructed from the 3D fetal brain MRI reconstruction and immersed in an organic solvent. Immersion causes solvent imbibition into the surface of the physical gel which swells leading to a compressive strain in the outer layers that causes the surface layer to form convolutions that resemble the folding patterns in the brain cortex layer. Time-lapse images of the gel model to mimic brain folding in *Macaca mulatta* (rhesus macaque) up to G110 are shown in Fig. 2(a), while in Fig. 2(b), we show the initial and final states of swelling to mimic different post-gestation stages corresponding to G85, G110 and G135. A visual inspection of the swollen gels constructed from different post-gestation stages showed qualitatively different folding patterns, indicating the sensitivity of the folds to the initial undulations present on the physical gel surfaces. In Fig. 2(c) and Movie S1, we show the results of similar physical gel experiments to mimic brain folding morphogenesis for *Homo sapiens* [22] and *Mustela furo* [11]; in each case the initial condition was based on 3d fetal brain MRIs and the final state was determined qualitatively using the overall volume of the brain relative to the initial state. No

attempt was made to vary the swelling ratio of the surface as a function of location, although it is likely that in the different species this was not a constant. To quantitatively describe the folding patterns, the swollen gel surfaces were then scanned and reconstructed using X-ray Computed Tomography (Methods). Movie S2–S4 showed the fetal brain MRI scans and the reconstructed 3D swollen gel surfaces in juxtaposition for *H. sapiens*, *M. furo*, and *M. mulatta*. This paves the way for a quantitative comparison of the results of the physical experiments with those derived from a mechanical theory for brain morphogenesis and those from scans of macaque, ferret and human brains.

Simulations of growing brains

To test the capability of the mechanical model for brain morphogenesis based on differential growth [21, 28, 22] to explain patterns across species, we perform numerical simulations of the developing brains of ferret, macaque, and human modeled as soft tissues. Here we only consider the simplest homogeneous growth profile which is sufficient to capture the folding formation across different species; regional growth of the cortical layer based on real data from tracking the surface expansion of fetal brains [29, 30, 31] is a more sophisticated alternative that we do not adopt for reasons of simplicity. The initial brain models are reconstructed from 3D fetal brain MRI (*Methods*), and assumed to be composed of gray and white matter layers which are considered as hyperelastic materials with differential tangential growth ratio g. A multiplicative decomposition of deformation gradient gives $\mathbf{F} = \mathbf{A} \cdot \mathbf{G}$ with $\mathbf{A}$ the elastic part and $\mathbf{G} = \sqrt{g}\mathbf{I} + (1 - \sqrt{g})\mathbf{n} \otimes \mathbf{n}$ the growth tensor. We adopt a modestly compressible neo-Hookean material with strain energy density

$$W = \frac{\mu}{2}\left[J_{\mathrm{A}}^{-2/3}\mathrm{tr}(\mathbf{A}^{\mathrm{T}} \cdot \mathbf{A} - 3)\right] + \frac{K}{2}\left(J_{\mathrm{A}} - 1\right)^2, \tag{1}$$

where $\mathbf{F}$ is the deformation gradient, $J_{\mathrm{A}} = \det\mathbf{A}$, μ is the initial shear modulus, and K is the bulk modulus. Considering modestly compressible material, we assume $K = 5\mu$.

We solve the final shapes of the growing tissues using a custom finite element method [22]. All the initial geometries of smooth fetal brains are obtained from open data sources (*Methods*, 3D model reconstruction), and the growth ratio distribution is assumed as a function of the initial

location, including the distance to the cortical surface and the presumably non-growing regions. Other parameters, such as the thickness ratio and modulus ratio of gray and white matter, and the temporal changes of growth ratios are assumed (*Methods*, numerical simulations, Table 2). The brain models are discretized to tetrahedrons by Netgen. An explicit algorithm is adopted to minimize the total strain energy of the deforming tissues. We adopt a step-wise simulation strategy where the initial geometry of each presumed stress-free state is obtained from real MRI data of earlier-stage fetal brains, instead of using a continuous model where only the initial smooth brain geometry is input [22]. The simulated developmental processes of fetal brains are presented in Fig. 3 and Movie S1.

Morphometric analysis

To verify whether our simulation methods and physical gel models are sufficient to capture the developmental process of fetal brains and reproduce cortical patterns in adult brains, we compare the cortical surfaces of real, simulated, and gel brains across different species. Fig. 4(a) presents the hemispherical cortical surfaces of the real, simulated, and gel brains (denoted as $\mathcal{S}_1$, $\mathcal{S}_2$, and $\mathcal{S}_3$, respectively). Left and right symmetry and the comparison of whole brains are presented in Fig. S3 and S4, Movie S2–S4. Major sulci are extracted and highlighted by hand for further alignment. To analyze the shape differences, we then adapted the parameterization methods in [32, 33, 34] to map the brain surfaces onto a common disk shape with the major sulci aligned using landmark-matching disk quasi-conformal parameterizations. Denote the three disk parameterization results as $\mathcal{D}_1, \mathcal{D}_2, \mathcal{D}_3$, as shown in Fig. 4(b). Multiple quantitative measures such as surface area, cortical thickness, curvature, and sulcal depth can be adopted to analyze curved surfaces and to compare different surfaces. Here, we use shape index (SI) and rescaled mean curvature $\tilde{H}$ to describe the similarity among real, simulated, and gel surfaces. Shape index is a dimensionless and scale-independent surface measure [35]. It can be calculated from the mean and Gaussian curvatures by

$$\mathrm{SI} = \frac{2}{\pi}\arctan\left(\frac{H}{\sqrt{H^2 - K}}\right). \tag{2}$$

Shape index ranging within $[-1, 1]$ defines a continuous shape change from convex, saddle, to concave shapes. Fig. S2 shows nine categories of typical curved surfaces. For brain surfaces,

we can classify sulcal pits ($-1 < \mathrm{SI} < -0.5$), sulcal saddles ($-0.5 < \mathrm{SI} < 0$), saddles($\mathrm{SI} = 0$), gyral saddles ($0 < \mathrm{SI} < 0.5$) and gyral nodes ($0.5 < \mathrm{SI} < 1$). When the shape index equals -1 or 1, it represents a defect of the curvature tensor with two eigenvalues identical, as shown in Fig. S3. The probability of shape index distribution exhibits two peaks, as shown in Fig. 4(c), corresponding to ridge and rut shapes (SI=± 0.5), where the ridge shape (SI= 0.5) is dominating. In contrast, the rescaled mean curvature histogram exhibits a unique peak around 0.2 (Fig. S3). The two-peak and unique-peak distributions of adult human brain surfaces have also been presented in previous research [36, 37]. To quantify the similarities between every two brain surfaces, we evaluate the distribution of $I(v)$ differences on the common disk domain at each vertex v. Here $I(v)$ represents either the surface shape index $\mathrm{SI}(v)$ or the rescaled mean curvature $\tilde{H}(v)$ defined as

$$\tilde{H}(v) = 2\frac{H(v) - \min(H)}{\max(H) - \min(H)} - 1. \tag{3}$$

Thus the similarity s of the distributions $I_{\mathcal{S}_1}, I_{\mathcal{S}_2}$ of the two surfaces $\mathcal{S}_1, \mathcal{S}_2$ is then evaluated via

$$s(\mathcal{S}_1, \mathcal{S}_2) = 1 - \frac{1}{2m^{1/p}} \left\| I_{\mathcal{S}_1} - I_{\mathcal{S}_2}(g_2^{-1} \circ f_{12} \circ g_1) \right\|_p, \tag{4}$$

where m is the total number of vertices, $g_1 : \mathcal{S}_1 \to \mathcal{D}_1$ and $g_2 : \mathcal{S}_2 \to \mathcal{D}_2$ are the initial disk conformal parameterizations, f_{12} is the landmark-aligned quasi-conformal map between $\mathcal{D}_1$ and $\mathcal{D}_2$, and $\| \cdot \|_p$ is the vector p-norm:

$$\left\| I_{\mathcal{S}_1} - I_{\mathcal{S}_2}(g_2^{-1} \circ f_{12} \circ g_1) \right\|_p = \left(\sum_{k=1}^{m} \left| I_{\mathcal{S}_1}(v_k) - I_{\mathcal{S}_2}((g_2^{-1} \circ f_{12} \circ g_1)(v_k)) \right|^p \right)^{1/p}. \tag{5}$$

Note that since $I_{\mathcal{S}_1} \in [-1, 1]$ and $I_{\mathcal{S}_2} \in [-1, 1]$, we have $0 \leq \left\| I_{\mathcal{S}_1} - I_{\mathcal{S}_2}(g_2^{-1} \circ f_{12} \circ g_1) \right\|_p \leq (2^p m)^{1/p} = 2m^{1/p}$. Therefore, we always have $0 \leq s(\mathcal{S}_1, \mathcal{S}_2) \leq 1$.

We calculate the similarity indices with different p-norm: $p = 1$, $p = 2$, and $p = \infty$ of both rescaled mean curvature and shape index. The results are given in Table 1 and Table S2.

Discussion

In this study, we have explored the mechanisms underlying brain morphogenesis for a few different mammalian species. Using fetal and adult brain MRIs for ferrets, macacques and

Table 1: Similarity index evaluated by comparing the shape index of simulated brains (S), swollen gel brain simulacrums (G) and real brain surfaces (R), calculated with vector p-norm $p = 2$, as described in Eq. (4).

Similarity Index	simulation-real	gel-real	simulation-gel
Ferret (left)	0.7632	0.7307	0.7117
Ferret (right)	0.7339	0.7222	0.7019
Macaque (left)	0.7624	0.7608	0.7512
Macaque (right)	0.7559	0.7632	0.7463
Human (left)	0.6947	0.7425	0.7000
Human (right)	0.6909	0.7325	0.7001

humans, we carried out physical experiments using swelling gels, combined with a mathematical framework to model the differential growth of the cortex that leads to iterations and variations of a mechanical (sulcification) instability that allowed us to recapitulate the basic morphological development of folds. We then deployed a range of morphometric tools to compare the results of our physical experiments and simulations with 3d scans of real brains, and show that our approaches are qualitatively and quantitatively consistent with experimental observations of brain morphologies.

All together, our study shows that differential growth between the gray matter cortex and white matter bulk provides a minimal physical model to explain the variations in the cortical folding patterns seen in multiple species. More specifically, we see that the overall morphologies are controlled by the relative size of the brain (compared to the cortex), as well as the scaled surface expansion rate, both of which can and do have multiple genetic antecedents [38, 39, 40, 41, 42] (see SI, Table S1). Our results point to some open questions. First, the relationship between physical processes that shape organs and the molecular and cellular processes underlying growth has been the subject of many recent studies, e.g. in the context of gut development [43, 44], and it would seem natural to expect similar relationships in brain development. There is a growing literature linking genes with brain malformation and pathologies. For example, GPR56 [38] and Cdk5 [39] can affect progenitors and neurons in migration, SP0535 [40] can affect neural proliferation, and foxpp2 can affect neural differentiation [41, 42], all of which change the cortical expansion rate and thickness, consequently leading to brain malformation and pathologies, as listed in Table S1. While a direct relation between gene expression levels and the effective

tangential growth rate $\mathbf{G}$ and cortical thickness has only been partially resolved, as for example in our companion study on the folding and misfolding of the ferret brain [11], further studies are needed to address how genetic programs drive cell proliferation, migration, size and shape change that ultimately lead to different cortical morphologies. Second, although our focus has been exclusively on the morphology of the brain, recent studies [3, 12] are suggestive of a link between cortical geometry and function from both developmental and evolutionary perspectives, and suggest natural questions for future study. Third, we are not able to set a spatio-temporal distribution of the cortical expansion for fetal brain surfaces of all three species because of a lack of growth rate data *in vivo*. The effect of inhomogeneous growth needs to be further investigated by incorporating regional growth of the gray and white matter not only in human brains [29, 31], but also in other species. Finally, our physical and computational models along with our morphometric approaches are a promising avenue to pursue in the context of the inverse growth problem, i.e., postulate the fetal brain morphologies from the adult brains. This may one day soon allow us to reconstruct the adult brain geometries from fossil endocasts [45], and eventually provide insights into how a few mutations might have triggered the rapid expansion of the cortex across evolutionary time and led to the highly convoluted human brain that is able to ponder the question of how it might have folded itself.

Methods

3D model reconstruction

Pre-processing

We used a publicly available database for all our 3d reconstructions: fetal macaque brain surfaces are obtained from [26]; newborn ferret brain surfaces are obtained from [11]; and fetal human brain surfaces are obtained from [22]. These 2D manifolds of brain surfaces were first normalized by their characteristic lengths $L_0 = L_x^0/2$ and discretized to triangle meshes by Meshlab [46] and then converted to 3D models and discretized to tetrahedral elements in Netgen [47].

Post-processing

All the numerically calculated brain surfaces and scanned gel brain surfaces were extracted as 3D triangle meshes. These intact cortical surfaces were then dissected to left and right semi-brains

and normalized by half of their longitudinal lengths $L = L_x/2$. These surfaces were then checked and fixed to a simply connected open surface to satisfy the requirements for open disk conformal mapping [32].

Experimental protocol for gel experiments The physical gel was constructed following a previous publication [22]. In brief, a negative rubber mold was generated with Ecoflex 00-30 from a 3D-printed fetal brain plastic model. The core gel was then generated with SYLGARD 184 at a 1:45 crosslinker: base ratio. Three layers of PDMS gel at a 1:35 crosslinker:base ratio were surface-coated onto the core layer to mimic the cortex layer. Pigments were added to the PDMS mixture for bright-field visualization. To mimic the cortex folding process, the physical gel was immersed in n-hexane. The time-lapse videos were taken with an iPod Touch 7th Gen. To reconstruct the swollen gel surface and analyze the folding patterns, swollen gels were imaged with a Nikon X-Tek HMXST X-ray CT machine. The voxel resolution for all scans was 100 μm. To minimize solvent evaporation during the 30-minute scan, cotton soaked in the solvent was placed inside the container. The container's thin acrylic walls allowed for clear X-ray transmission. The container's thin acrylic walls allowed for clear X-ray transmission. To test the reversibility of the folding pattern formation, the physical gel models were allowed to dry in a laminar flow hood overnight before being immersed in hexane again.

3D reconstruction of swollen gel surface from X-ray CT The z-stack images obtained from the X-ray CT machine were segmented by a machine-learning-based segmentation toolbox, Labkit, via ImageJ. A classification was created for each swollen gel. Then a 3D surface of the segmented gel image was generated by ImageJ 3D viewer. Further post-processing was conducted in SOLIDWORKS and MeshLab, including reversing facial normal direction, re-meshing, and surface-preserving Poisson smoothening.

Numerical Simulations The simulation geometries of ferret, macaque, and human are based on MRI of smooth fetal or newborn brains. For ferret, we take the P0, P4, P8, and P16 fetal brains as initial shapes of the step-wise growing model; for macaque, we take G80 and G110 fetal brains as initial shapes of the step-wise growing model; and for human, we take GW22

Table 2: Parameters for numerical simulations

species	model	$g_{\mathrm{g}}/g_{\mathrm{w}}$	$\mu_{\mathrm{g}}/\mu_{\mathrm{w}}$	h/L
Ferret	step-wise	1.8	1	$0.1 - 0.005t$
Macaque	step-wise	1.8	1	$0.1 - 0.05t$, $0.1 - 0.1t$
Human	continuous	1.8	1	$0.05 - 0.03t$

fetal brain as the initial shape of the continuous growing model. Both gray and white matter are considered as neo-Hookean hyperelastic material with the shear modulus distribution

$$\mu(d) = \mu_{\mathrm{w}} + \frac{\mu_{\mathrm{g}} - \mu_{\mathrm{w}}}{1 + \exp[10(d/h - 1)]}, \tag{6}$$

where d is the distance from an arbitrary material point inside the brain to the cortical surface, and h is the approximated cortical thickness assumed to decrease with growth process time t [22]. The subscripts 'g' and 'w' represent gray and white matter, respectively. The tangential growth ratio g has a similar spatial distribution

$$g(d) = g_{\mathrm{w}} + \frac{g_{\mathrm{g}} - g_{\mathrm{w}}}{1 + \exp[10(d/h - 1)]}, \tag{7}$$

where g_{w} and g_{g} represent the growth ratio at cortical surface and at innermost white matter. The parameters used in simulations are listed in Table 2.

Data availability

Reconstructed 3D surface models of fetal and adult brains of macaque and human are available on GitHub at https://github.com/YinSifan0204/Comparative-brain-morphlogies. Newborn ferret brain surfaces will be made available upon publication of the paper. All other data are included in the article and/or supplementary material.

Author contributions

L.M. and R.T. conceived the project; S.Y., C.L., G.P.T.C., and L.M. designed research; S.Y. collected data and performed numerical simulations; C.L. and Y.J. performed gel experiments; S.Y. and G.P.T.C contributed morphometric analysis; K.H. and R.T. provided adult ferret and primate brain data; S.Y., G.P.T.C., and L.M. wrote the paper with input from all authors; all authors edited the paper; L.M. supervised the project.

Acknowledgements

We acknowledge partial financial support from project NeuroWebLab (ANR-19-DATA-0025, K.H., R.T.), DMOBE (ANR-21-CE45-0016), the European Union's Horizon 2020 research and innovation programme under the Marie Skłodowska-Curie grant agreement 101033485 (K.H. Individual Fellowship), the NSF-ANR grant 2204058 (K.H., R.T., L.M.), the Simons Foundation (L.M.) and the Henri Seydoux Fund (L.M.), and the CUHK Faculty of Science Direct Grant for Research #4053650 (G.P.T.C.).

Competing interests

The authors declare no conflict of interest.

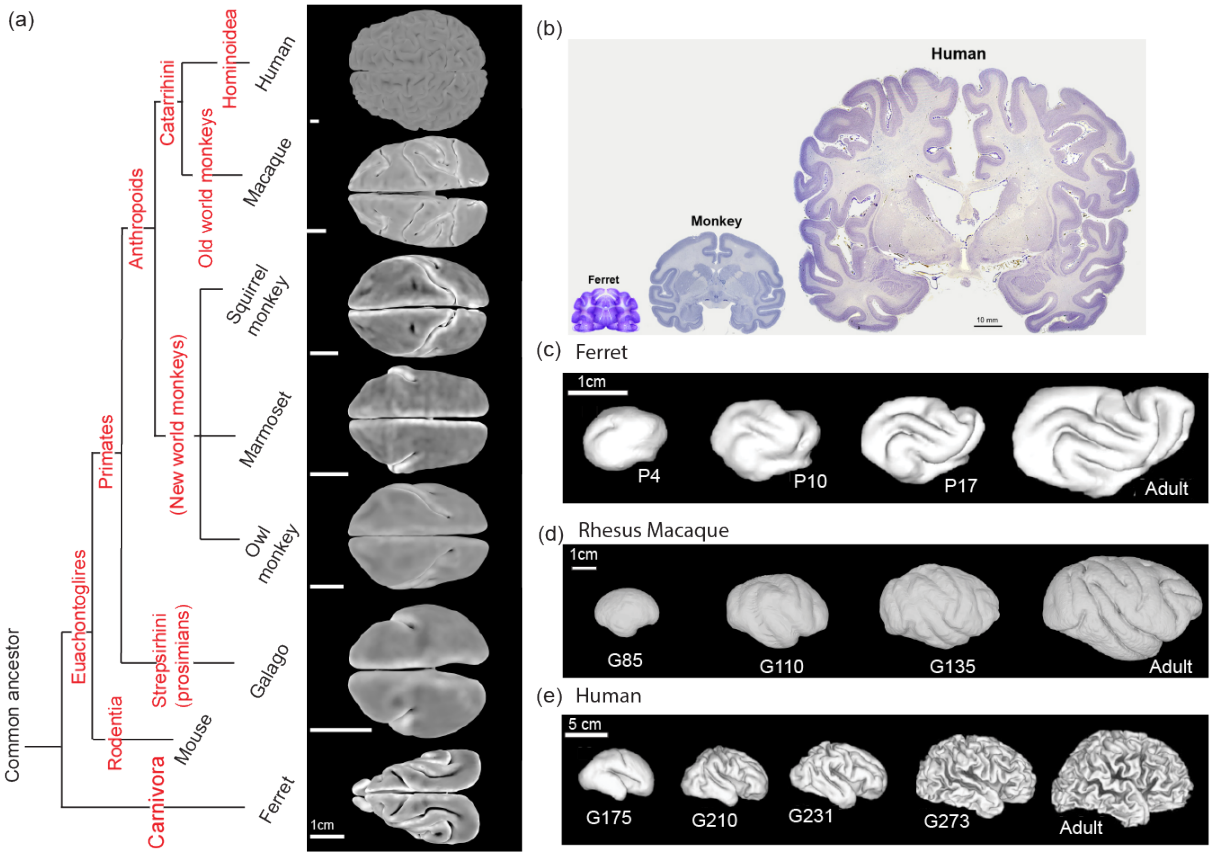

Fig. 1: **The diversity of the cortical morphologies and developmental processes across species.** (a) Phylogenetic relationship of species. Adapted from [6, 7]. Typical real brain surfaces of ferret and primates are presented. Color represents mean curvature. Scale bars: 1 cm (estimated from [23]). (b) Stained sections of mature brain tissue from ferret, rhesus macaque, and human. Scale bar: 10 mm. Adapted from [24]. (c-e) 3D reconstruction of cortical surfaces of ferret, macaque, and human brains from fetal to adult. (c) Ferret: postnatal day 4, 10, 17 and adult maturation [25]. Scale bar: 1cm; (d) Macaque: gestation day 85, 110, 135 [26], and adult maturation [27]. Scale bar: 1cm; (e) Human: gestation day 175 (week 25), 210 (week 30), 231 (week 33), 273 (week 39), and adult maturation [25]. Scale bar: 5cm.

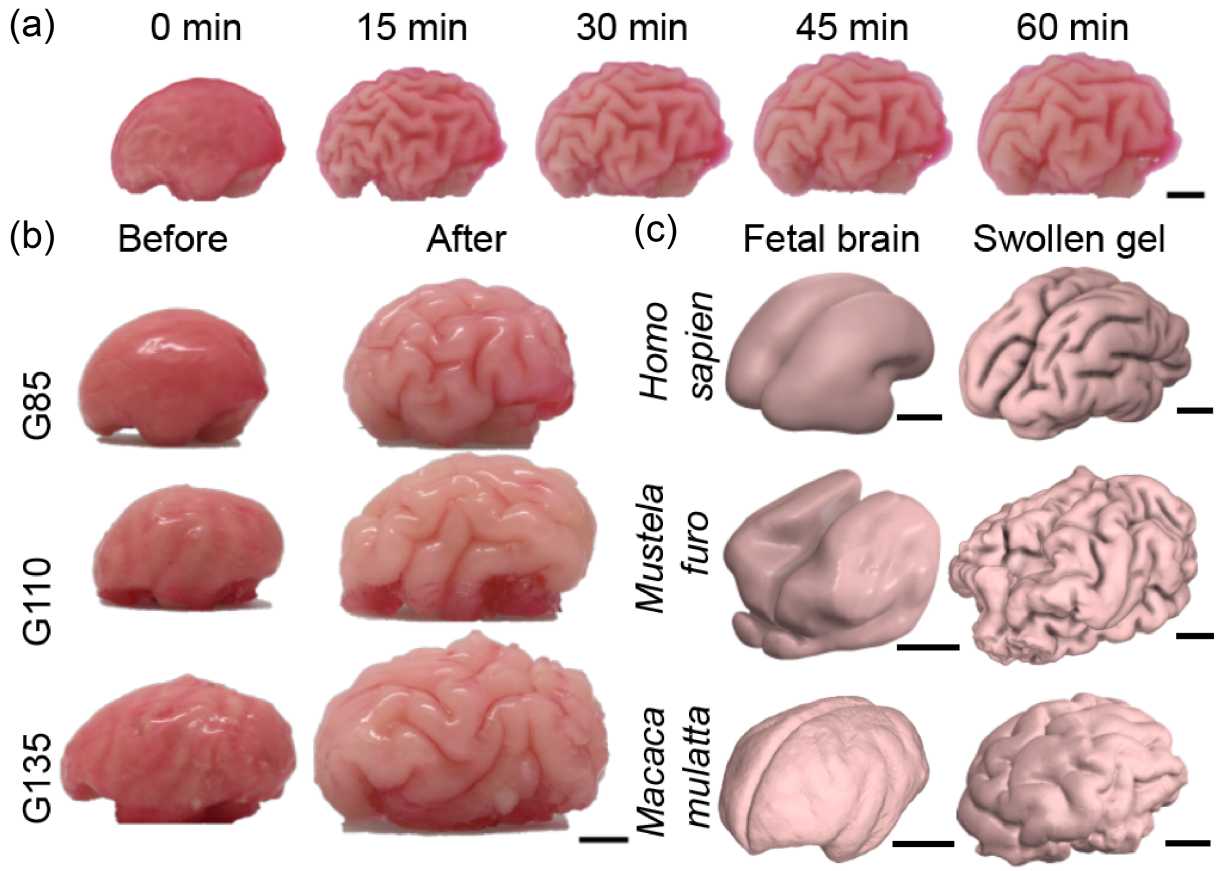

Fig. 2: **Physical gel model that recapitulates the growth-driven morphogenesis mechanism across phylogeny and developmental stages.** (a) A time-lapse of the physical gel brain mimicking macaque brain development starting from G110. (b) Left views of three physical gels mimicking macaque post gestation day 85, day 110, and day 135 before and after hexane swelling. Scale bar: 1 cm. (c) Comparison of fetal/newborn brain scans and the reconstructed surfaces of swollen physical gels for various species. Scale bars: 1 cm.

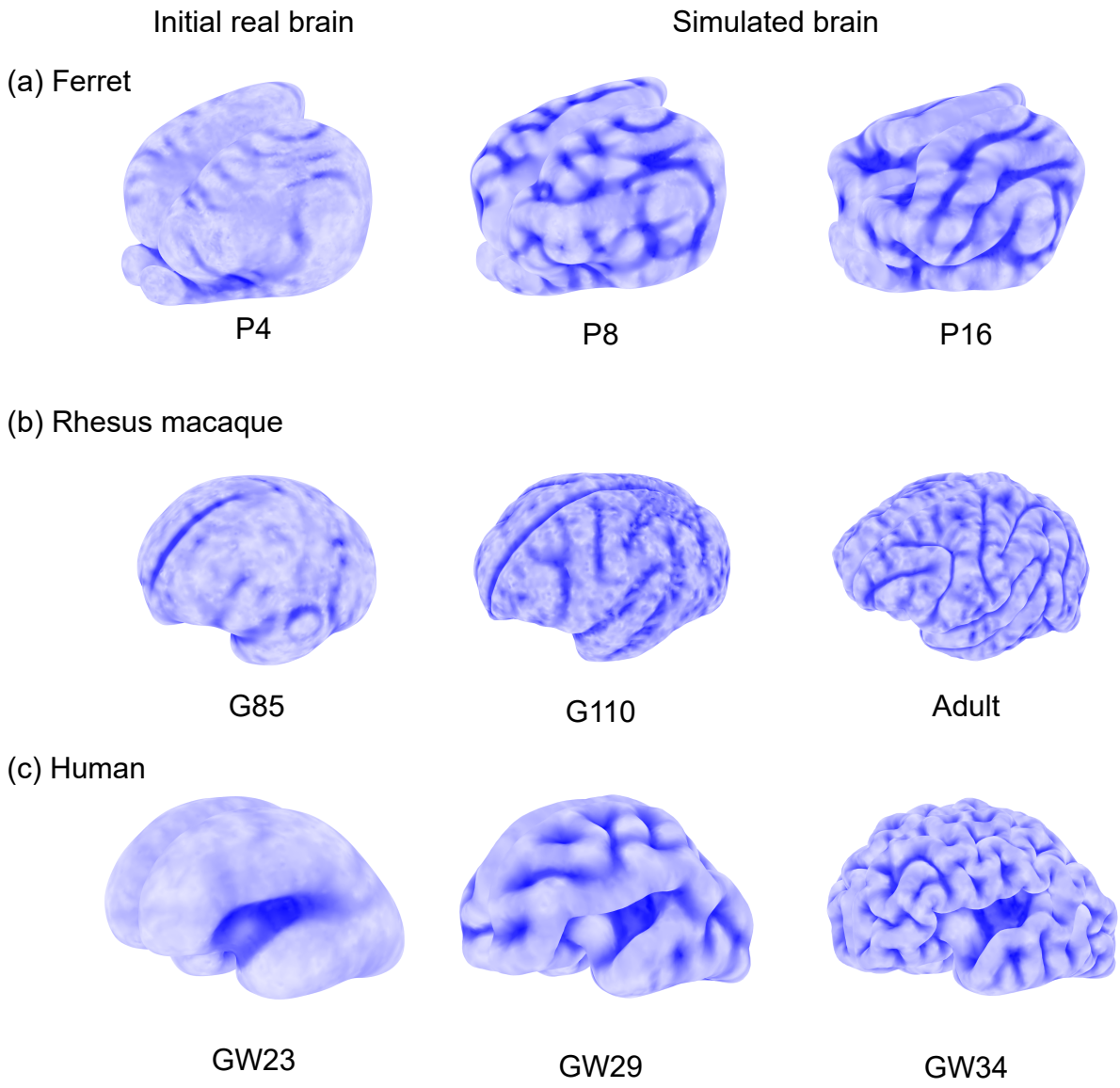

Fig. 3: **Simulations of growing brains** of (a) ferret, (b) rhesus macaque, and (c) human. Starting from smooth fetal/newborn brains, simulations show different gyrification patterns across species. The brains are modeled as soft elastic solids with tangential growth in the gray matter (see *Simulations of growing brains* for details). Initial 3D geometries are taken from the reconstruction of MRI (see *Methods*, 3D model reconstruction). Mechanical parameters of growth ratio and cortical thickness are provided in Table 2. Color from dark to light blue represents shape index (as defined in Eq. (2)) from -1 to 1.

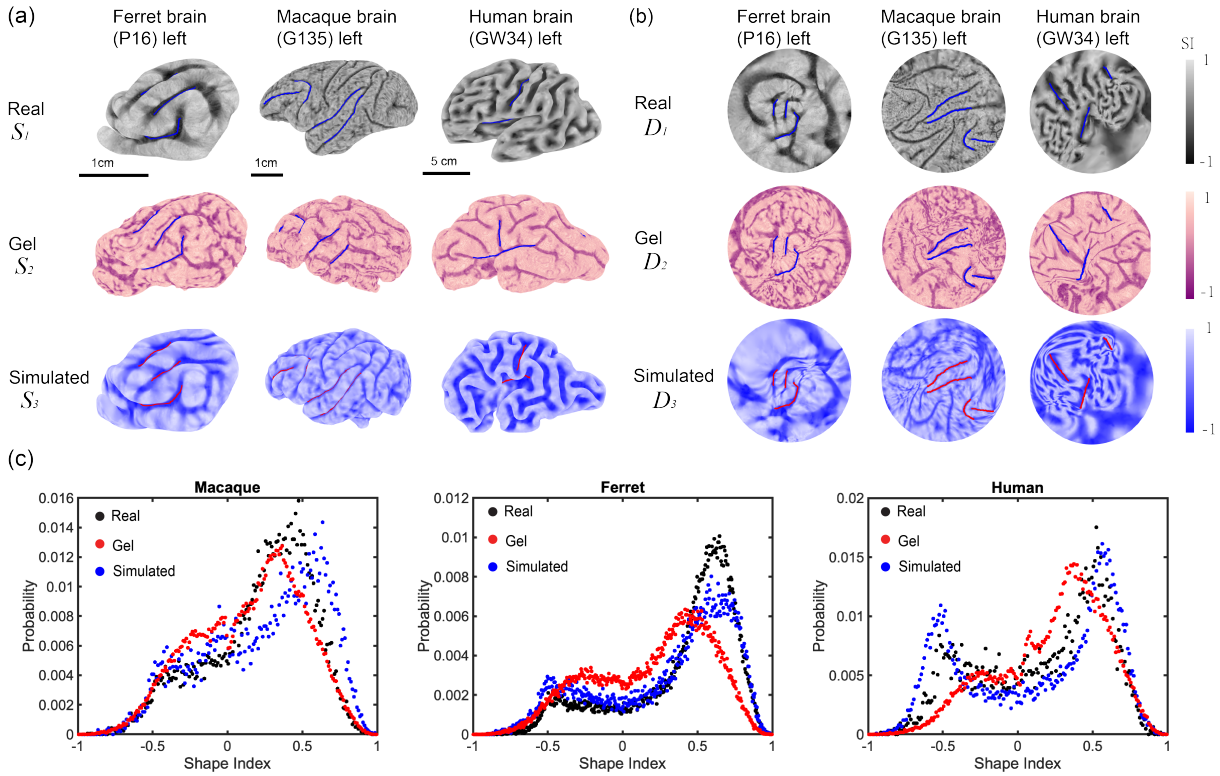

Fig. 4: **Comparison among real ($\mathcal{S}_1$), simulated ($\mathcal{S}_2$), and gel brains ($\mathcal{S}_3$) of ferret, rhesus macaque, and human via morphometric analysis.** (a) 3D cortical surfaces of *in vivo*, *in silico*, and *in vitro* models. Left brain surfaces are provided here. The symmetry of the left and right halves of brain surfaces is discussed in Fig. S3 and S4, Movie S2–S4. (b) The quasi-conformal disk mapping with landmark matching of cortical surfaces on disk (see Sec *Morphometric analysis* for details). Blue or red curves represent corresponding landmarks. Color represents shape index (SI, as defined in Eq. (2)). Similarity indices of each simulated and gel brain surfaces are presented in Table 1. (c) Histogram of shape index of ferret, macaque, and human. Black, red, and blue dots represent the probability of shape index of real, gel, and simulated surfaces, respectively.

References

[1] P. Gautam, K. J. Anstey, W. Wen, P. S. Sachdev, N. Cherbuin, *Behavioural Brain Research* **287**, 331 (2015).

[2] L. E. Suárez, R. D. Markello, R. F. Betzel, B. Misic, *Trends in Cognitive Sciences* **24**, 302 (2020).

[3] J. C. Pang, *et al.*, *Nature* **618**, 566 (2023).

[4] E. T. Bullmore, D. S. Bassett, *Annual Review of Clinical Psychology* **7**, 113 (2011).

[5] N. Kriegeskorte, X.-X. Wei, *Nature Reviews Neuroscience* **22**, 703 (2021).

[6] T. Takahata, R. Shukla, T. Yamamori, J. H. Kaas, *Cerebral Cortex* **22**, 2313 (2012).

[7] K. Heuer, *et al.*, *Cortex* **118**, 275 (2019).

[8] C. Hutton, B. Draganski, J. Ashburner, N. Weiskopf, *Neuroimage* **48**, 371 (2009).

[9] F. H. P. de Moraes, *et al.*, *Scientific Reports* **14**, 3222 (2024).

[10] R. Oegema, *et al.*, *Nature Reviews Neurology* **16**, 618 (2020).

[11] G. P. T. Choi, *et al.*, *Preprint* (2025).

[12] E. Schwartz, *et al.*, *Nature Communications* **14**, 2252 (2023).

[13] D. van der Meer, T. Kaufmann, *Translational Psychiatry* **12**, 447 (2022).

[14] L. Del-Valle-Anton, V. Borrell, *Physiological Reviews* **102**, 511 (2022).

[15] S. K. Akula, D. Exposito-Alonso, C. A. Walsh, *Developmental Cell* **58**, 2836 (2023).

[16] G. F. Striedter, S. Srinivasan, E. S. Monuki, *Annual Review of Neuroscience* **38**, 291 (2015).

[17] M. A. Holland, K. E. Miller, E. Kuhl, *Annals of Biomedical Engineering* **43**, 1640 (2015).

[18] D. C. Van Essen, *Proceedings of the National Academy of Sciences* **117**, 32868 (2020).

[19] E. Hohlfeld, L. Mahadevan, *Physical Review Letters* **106**, 105702 (2011).

[20] T. Tallinen, J. S. Biggins, L. Mahadevan, *Physical Review Letters* **110**, 024302 (2013).

[21] T. Tallinen, J. Y. Chung, J. S. Biggins, L. Mahadevan, *Proceedings of the National Academy of Sciences* **111**, 12667 (2014).

[22] T. Tallinen, *et al.*, *Nature Physics* **12**, 588 (2016).

[23] S. Herculano-Houzel, *Frontiers in Human Neuroscience* **3**, 857 (2009).

[24] Comparisons, 2, `https://ventricular.org/StephenNoctor/comparisons-2/` (2016).

[25] A. R. Barnette, *et al.*, *Pediatric Research* **66**, 80 (2009).

[26] Z. Liu, *et al.*, *Neuroimage* **206**, 116310 (2020).

[27] E. Calabrese, *et al.*, *Neuroimage* **117**, 408 (2015).

[28] S. Budday, C. Raybaud, E. Kuhl, *Scientific Reports* **4**, 5644 (2014).

[29] K. E. Garcia, *et al.*, *Proceedings of the National Academy of Sciences* **115**, 3156 (2018).

[30] M. Alenyà, *et al.*, *Brain Multiphysics* **3**, 100045 (2022).

[31] J. Weickenmeier, *Brain Multiphysics* **4**, 100068 (2023).

[32] P. T. Choi, L. M. Lui, *Journal of Scientific Computing* **65**, 1065 (2015).

[33] P. T. Choi, K. C. Lam, L. M. Lui, *SIAM Journal on Imaging Sciences* **8**, 67 (2015).

[34] G. P. T. Choi, Y. Leung-Liu, X. Gu, L. M. Lui, *SIAM Journal on Imaging Sciences* **13**, 1049 (2020).

[35] J. J. Koenderink, A. J. van Doorn, *Image and Vision Computing* **10**, 557 (1992).

[36] N. Demirci, M. A. Holland, *Human Brain Mapping* **43**, 2064 (2022).

[37] H.-H. Hu, H.-Y. Chen, C.-I. Hung, W.-Y. Guo, Y.-T. Wu, *Brain Structure and Function* **218**, 1451 (2013).

[38] B.-I. Bae, *et al.*, *Science* **343**, 764 (2014).

[39] Y. Shinmyo, *et al.*, *Cell Reports* **20**, 2131 (2017).

[40] J. Qi, *et al.*, *Advanced Science* **10**, 2204140 (2023).

[41] C. S. Lai, D. Gerrelli, A. P. Monaco, S. E. Fisher, A. J. Copp, *Brain* **126**, 2455 (2003).

[42] M. Barresi, *et al.*, *Cerebral Cortex* **34**, bhae055 (2024).

[43] H. K. Gill, *et al.*, *Proceedings of the National Academy of Sciences* **121**, e2310992121 (2024).

[44] H. K. Gill, *et al.*, *Developmental Cell* **59**, 2834 (2024).

[45] A. A. de Sousa, *et al.*, *Communications Biology* **6**, 636 (2023).

[46] P. Cignoni, *et al.*, *Eurographics Italian Chapter Conference* (Salerno, Italy, 2008), vol. 2008, pp. 129–136.

[47] NetGen, `https://ngsolve.org/` (2019).